TEMPERATURE FIELDS ANALYSIS AND HEAT DISSIPATION STRUCTURE DESIGN OF AN FILM CAPACITOR IN NEW ENERGY VEHICLE

by

Bin CHANG[1], Tao YUAN[1,*], Yansong WANG[1,*], Zhanghao LI[2], Hui GUO[1], Linhao HUANG[1], and Lihui ZHAO[3]

[1] School of Mechanical and Automotive Engineering, Shanghai University of Engineering Science, Shanghai, China

[2] Guangzhou Junyi Electronics Technology Co., Guangzhou, China

[3] School of Mechanical Engineering, University of Shanghai for Science and Technology, Shanghai, China

[*] Corresponding author: E-mail: taoyuan2016@gmail.com, jzwbt@163.com

The high-temperature resistance performance of film capacitors in motor controllers faces greater challenges with the development of high voltage and high power density of new energy vehicles (NEVs). In this study, a typical film capacitor is taken as the object of research; simulations of temperature fields and experiments on temperature rises are conducted. Additionally, a heat dissipation structure is designed to enhance the high-temperature resistance performance of the capacitor. Firstly, the temperature field distributions of the capacitor under different ripple currents and ambient temperatures are analyzed using ANSYS electro-thermal coupling simulation. Then, under the same operating conditions, experiments on the temperature rises are conducted on the capacitor, which is installed with K-type thermocouples to verify the accuracy of the electro-thermal coupling simulation. Furthermore, an external heat dissipation structure consisting of a micro-channel liquid cold plate is designed for the capacitor, and the effectiveness of the external cold plate is verified through electro-thermal coupling and FLUENT simulations. It is found that under the operating conditions of 85 °C ambient temperature and 175 A ripple current, the maximum temperature of the capacitor with the external cold plates decreases by 46.08% compared to the original capacitor. The results indicate that the external cold plates effectively improve the high-temperature resistance capability of the film capacitors in electric vehicles.

Key words*: Film Capacitor, Temperature field, High-temperature resistance, Electro-thermal coupling, Micro-channel liquid cold plate*

1. Introduction

In an era marked by heightened attention to energy resources and a sustained commitment to environmental conservation, emerging technologies in the automotive sector, particularly new energy vehicles (NEVs) including electric vehicles (EVs) and hybrid vehicles, have assumed a central role.

These vehicles symbolize a crucial step toward fostering high-quality and sustainable development within the automotive industry[1,2]. As a pivotal aspect of NEVs, the trajectory of motor controller development is progressively shifting towards high voltage and high power density. This evolution necessitates heightened standards for the heat resistance capabilities of power modules and components, reflecting the industry's growing demand for robust performance under elevated temperatures [3]. Film capacitors constitute more than 30% of the spatial allocation within motor controllers, assuming a pivotal function in managing ripple currents and ensuring the stable operation of motor controllers [4]. Silicon Carbide (SiC)-based Me tal-Oxide-Semiconductor Field-Effect Transistor (MOSFET) power modules have emerged as a significant technological advancement within the realm of electric and hybrid vehicles. In contrast to conventional Silicon-based Insulated Gate Bipolar Transistor (IGBT) power modules, SiC MOSFET power modules present notable advantages, including reduced switching and conduction losses. Consequently, they enhance the performance of motor controllers, particularly during high-power output scenarios, and facilitate more efficient operations[5,6]. The high-efficiency operation of SiC MOSFET power modules can subject other components within the motor controller, particularly capacitors, to heightened operating temperatures and more demanding working environments. Such elevated temperatures may trigger performance deterioration or even capacitor failure, consequently jeopardizing the stability and reliability of the entire electric vehicle system [7]. It is noteworthy that film capacitors generally uphold stable electrical performance when operating within conditions where the maximum internal temperature remains below 105°C [8,9]. However, as advancements in motor controller development yield higher power densities, there arises a necessity to engineer film capacitors with elevated temperature resistance grades.

Currently, efforts to enhance the temperature resistance grade of capacitors for NEVs are primarily concentrated on several fronts. Firstly, researchers are dedicated to developing high-temperature-resistant materials. Yang et al. proposed a method for fabricating flexible inorganic film capacitors, aiming to bestow the capacitors with elevated fatigue resistance and a broader operating temperature range [10,11]. Secondly, improvements in film structure are under exploration. Cui et al. conducted thermal resistance simulations for T-shaped safety films and diamond-shaped safety films, assessing the power density of the films based on equivalent resistance. Simulated analyses were performed on the overall temperature rise of capacitors. The outcomes suggest that while the thermal resistance of conventional metallized films is the lowest, the thermal resistance and equivalent resistance of safety films primarily hinge on the effective cross-sectional area of the fuse. As this area increases, thermal resistance diminishes, thereby enhancing the heat dissipation capability of capacitors [12,13]. However, it is noted that setting the ambient temperature to 25°C during thermal simulation may not accurately reflect real-world conditions. Thirdly, advancements in manufacturing processes are being explored. Li and Wu et al. devised an expandable high-temperature capacitor film using grafted polypropylene. This process involves continuous grafting of polypropylene, followed by melt casting, extrusion, and biaxial stretching to yield thin and uniform capacitor films [14,15]. Nevertheless, this method presents challenges as it's incompatible with existing production processes and entails high raw material costs. These three aspects predominantly center on the material aspects of film capacitors, albeit with limited flexibility and applicability. Further development is warranted to address these constraints and advance the field. Introducing heat dissipation structures for capacitors facilitates swift integration into existing capacitor configurations once the design scheme is determined, swiftly enhancing capacitor heat dissipation performance. Compared to material modification, this approach offers advantages in terms of rapid implementation and cost-effectiveness. Several studies on capacitor thermal aging, thermal distribution, and heat dissipation structure design have been conducted by various research teams. Film capacitors endure varied electrical and thermal stresses, impacting their performance to differing extents based on the quality of dielectric materials and capacitor structures. MacDonald et al. [16] examined the pulse life and DC life of single-wound model capacitors, single-stack capacitors, and capacitors rated at 50 kJ, 100 kJ and 260 kJ. Notably, significant increases in leakage current and reductions in breakdown strength were observed in biaxially oriented polypropylene (BOPP) dielectrics under high-temperature conditions, resulting in rapid decreases in energy density and charge-discharge efficiency [17]. Yao and Kong et al. proposed a model for the heat transfer of metallized film capacitors, enabling the identification of local hot spots based on accumulated energy within the capacitors. The study revealed that capacitor lifespan increases as voltage and temperature decrease [18,19], however, measures to mitigate local hot spot temperatures were not proposed. Presently, there is relatively scant research on heat dissipation structures for film capacitors. In practical applications, most companies enhance capacitor heat dissipation by designing casings with fins or substituting casing materials with metals. Additionally, some companies dissipate heat from within the capacitor to the exterior by incorporating copper plates inside the casing or externally inserting copper plates [20,21]. Nevertheless, a notable gap remains in the absence of heat dissipation structures designed based on internal capacitor temperature distributions.

Therefore, this study aims to investigate the internal temperature distribution patterns of film capacitors under various operating conditions and propose a microchannel liquid cooling plate structure for effective heat management in DC bus film capacitors. The primary focus is on exploring the high-temperature resistance performance of film capacitors in the context of NEVs. Through the utilization of finite element software ANSYS and temperature rise experiments, an electro-thermal coupling model of the capacitor will be established and validated. Subsequently, an external microchannel liquid cooling plate will be designed, and the electro-thermal coupling characteristics of the capacitor, along with the effectiveness of the proposed heat dissipation structure, will be thoroughly examined using FLUENT computational fluid dynamics software. This research endeavors to offer valuable insights into the thermal management and optimization of film capacitors, potentially contributing to the advancement of film capacitor technology in future NEVs.

2. Film capacitor structure and core heat density calculation

2.1 Film capacitor structure

The film capacitor model examined in this paper is 800 VDC-420 μF. It comprises capacitor cores, busbars, epoxy filling material, and a casing, with overall dimensions of 268 mm×102 mm×96 mm, as illustrated in fig. 1.The resistances of the metal components, such as the busbar, the connecting solder points, and the sprayed metal layers of the cores, are collectively referred to as the equivalent series resistance (ESR) of the capacitor. Film capacitors used in NEVs are generally metallized film capacitors. Under high environmental temperatures and inadequate heat dissipation conditions, metallized film capacitors may experience failures and even lead to serious issues such as explosions[22].

2.2 Calculation of core heat density

Figure 2 presents a schematic overview of a NEV powertrain, including the equivalent circuit of a film capacitor. In fig. 2, i_1 is the direct current output from the battery, i_2 is the current entering the inverter, i_3 is the ripple current of the capacitor. The relationship between i_1 and i_3 is determined by the impedance ratio, and $i_2=S_a i_a+ S_b i_b+ S_c i_c$, where S_a, S_b and S_c are the inverter's three-phase switching functions, i_a, i_b and i_c are the three-phase currents output by the inverter, respectively.

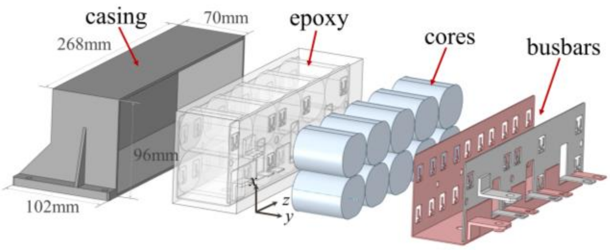

Figure 1. Structure of capacitor

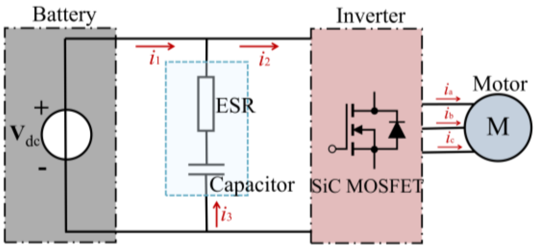

Figure 2. Equivalent circuit of film capacitor

In metallized film capacitors, the current exhibits a linear distribution along the width direction of the metallized film. It reaches its maximum value at the edges where metallization is applied and decreases to its minimum value at the free edges. The heating power of the metal electrode is influenced by this current distribution and can be expressed as:

$$p=\int_0^{b_w} i_3^{\,2} dR_{xm} = \int_0^{b_w}\left(\frac{1}{b_w}x\right)^2 \frac{\beta}{L}dx \tag{1}$$

where R_{xm} is the resistance of the metallized film, b_w is the width of the film, L is the winding length, β is the sheet resistance of the metal electrode.

According to the principles of heat transfer, the heating power of the capacitor is:

$$P = I^2 ESR \tag{2}$$

The calculation formula of ESR is given as：

$$ESR=\frac{2\rho(3b_0+b_w)}{3d_m L} \tag{3}$$

where b_0 is the margin width of the film, d_m is the thickness of the metal electrode layer.

In this study, a film capacitor with 10 cores is selected as research object, the selection of a 10 cores film capacitor is based on its capacity to meet the high power and energy density requirements of electric vehicles, its feasibility for experimental analysis, and its effectiveness in providing a solid foundation for optimizing the cooling structure. The metallized polypropylene coating is aluminum foil with a resistivity of 2.65×10^{-8} Ω·m. The core size is 1696 mm²×52.2 mm. With 10 cores and a ripple current of 150 A, the ESR of the capacitor cores can be calculated as 0.5 mΩ. The heat density of the cores is calculated by eq.(4):

$$q_{\mathrm{H}} = \frac{P}{V} \tag{4}$$

where q_{H} is the heat density of the cores, and V is the equivalent total volume of the capacitor cores, and V=8.85 x 10^{-4} m^3, the heat density of the cores is calculated as q_{H}= 12707.38 W/m^3.

3. Electro-thermal coupling simulation and temperature rises experiment

3.1 Electro-thermal coupling simulation of capacitor

3.1.1 Modeling and meshing

The capacitor consists of 14 components, including 10 cores, 2 busbars, epoxy filling materials and casing. The material parameters for the components are shown in tab. 1. The element size of the capacitor model is 0.0005 m, and the total nodes and elements are 12371404 and 8890729, respectively, which meets the analysis requirements.

Table 1 Capacitor material parameters

Components	Thermal Conductivity [$Wm^{-1}K^{-1}$]	Density [kgm^{-3}]	Specific Heat Capacity [$Jkg^{-1}°C^{-1}$]
Casing	18	1650	1000
Core	x-0.1, y-0.5, z-0.2	910	1883
Busbar	400	8900	386
Filling material	58	1820	1340

3.1.2 Electro-thermal coupling analysis

The capacitor features 8 terminals, where high-voltage DC terminals A and B are connected to the positive and negative poles of the high-voltage battery, supplying the required DC voltage for the inverter. The current magnitude is set to ±200 A. Terminals C, D, E, F, G, and H are linked to SiC MOSFETs. The three-phase bridge of MOSFETs modulates the voltage output from the capacitor to drive the three-phase voltage for the motor. Current magnitudes for each terminal are detailed in tab. 2. Simulations in ANSYS provide the current values for each capacitor terminal and the current density on the busbars, as illustrated in fig.3.

Table 2 Current magnitude at each terminal of the capacitor

Simulation conditions	Terminal current value [A]							
	A	B	C	D	E	F	G	H
150A/85°C/3hrs	-200	200	-50	50	-50	50	-50	50
175A/85°C/3hrs	-200	200	-58.3	58.3	-58.3	58.3	-58.3	58.3

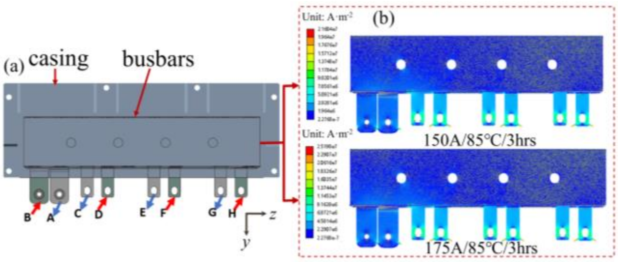

Figure 3. Current densities of the busbars

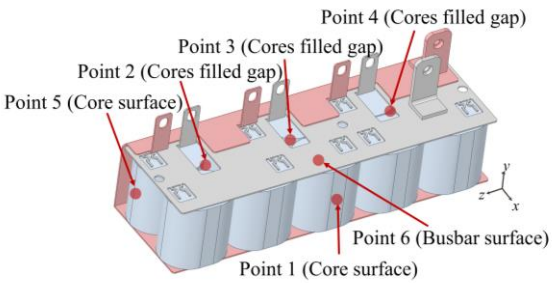

Figure 4. Measure points under 150 A

Based on the calculated heat density of the capacitor cores, an electro-thermal coupling analysis is performed using ANSYS. The simulation examines the temperature distribution of the entire capacitor under environmental temperatures of 85 °C with ripple currents of 150 A and 175 A. For the 150 A ripple current, six temperature measuring points are selected inside the capacitor, three locates inside the gaps between the cores ,two on the surfaces of the cores and one on the surfaces of the busbar, as illustrated in fig. 4. These points are analyzed to study the overall temperature distribution of the capacitor. For the 175 A ripple current, temperatures on the surfaces of the 10 cores are measured, as illustrated in fig. 5. Both sets of simulations under different operating conditions and measurement points will be validated through experiments. The simulation results of 150 A are illustrated in fig. 6, and the highest temperature of 100.88 °C is located on Point 4, which is near the high-voltage DC terminals A and B.

Through the electro-thermal coupling simulation, it can be observed that the highest temperature in the capacitor is located near the high-voltage DC terminals on the casing, while the lowest temperature is on the outer side of the casing. From an overall perspective of the capacitor, the casing has the lowest temperature, and the temperature distribution is irregular, with localized overheating areas. At the location near the DC input terminals on the casing, the temperature decreases from the input terminals towards the surroundings. The surface temperature near the DC input terminals is the highest. Therefore, designing a heat dissipation structure on the surface can effectively reduce the temperature of the capacitor, enhancing its high-temperature performance.

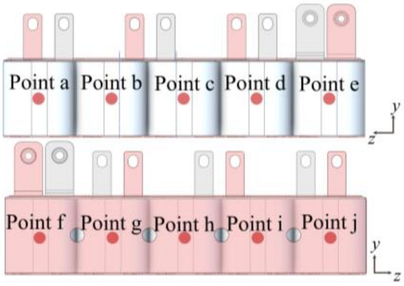

Figure 5. Measure points under 175 A

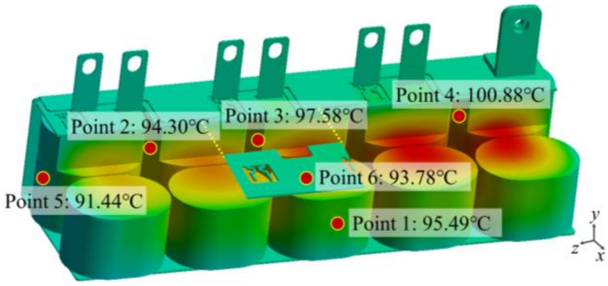

Figure 6. Temperature contour under 150 A

3.2 Temperature rises experiments of the capacitor

To further validate the accuracy of the ANSYS simulations, the capacitor was fabricated under conditions identical to the simulation, with ripple currents of 150 A and 175 A and an environmental temperature of 85 °C. A test system was established, as illustrated in fig. 7, comprising the high-frequency ripple current generator (fig.7(a)), the test capacitor (fig. 7(b) and 7(c)), arranged with K-type thermocouples at corresponding points as in the simulation, the temperature test chamber (fig. 7(d)), and a multi-channel temperature recorder (fig. 7(e)). The high-frequency ripple current generator provides ripple current to the capacitor with K-type thermocouples. The temperature test chamber maintains a stable environmental temperature for the capacitor. The multi-channel temperature recorder is used to record the results of K-type thermocouples.

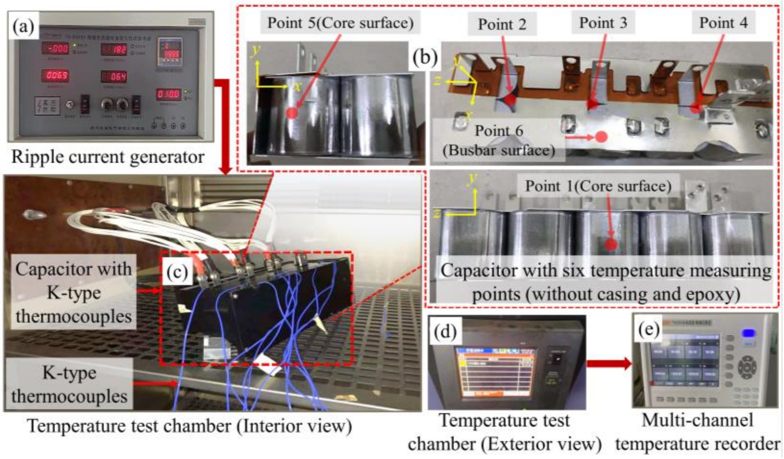

Figure 7. Capacitor temperature rise experiment system

3.3 Analysis of experimental results

In operating condition 1 (ripple current of 150 A, ambient temperature of 85 °C), fig. 8 displays the temperature rise at six points. For operating condition 2 (ripple current of 175 A, ambient temperature of 85 °C), fig. 9 shows the temperature rise on the surfaces of the 10 capacitor cores.

The effective values of the ripple currents input to the capacitor under operating conditions 1 and 2 are different. The test duration is 240 minutes, and at 130 minutes, the temperature rise curves of both tend to stabilize. In steady-state conditions, for operating condition 1, the simulation results at the six thermocouple locations are compared with the steady-state average of the experimental results. The comparison results are presented in tab. 3 and fig. 10. According to fig. 10, among the six measurement points, Point 4 has the highest average temperature, reaching 104.10 °C, for Point 4 is the closest to the high-voltage DC terminals A and B. The simulation percentage error between the temperature value at Point 4 and the experimental value is 1.10%. Point 5 has the lowest experimental average temperature, which is 87.52 °C, as it is relatively distant from the DC terminal. Among the six measurement points, the simulated temperature at Point 1 has the highest percentage error compared to the experimental temperature, at 4.65%. However, this percentage error still falls within the acceptable limit of 5%, confirming the credibility of the simulation results.

For operating condition 2, fig.9 displays the steady-state experimental results for the ten points on the surfaces of the cores. The simulation results for the same ten points under operating condition 2 are then compared with the steady-state average of the experimental results. The comparison results are illustrated in fig. 11. The results indicate that the percentage error of the simulated temperature values under both operating conditions is less than 5%, confirming the accuracy of the electro-thermal coupling simulation.

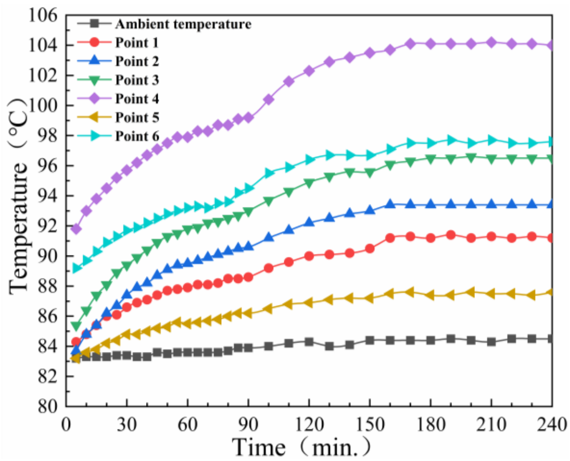

Figure 8. Temperature curves under 150 A

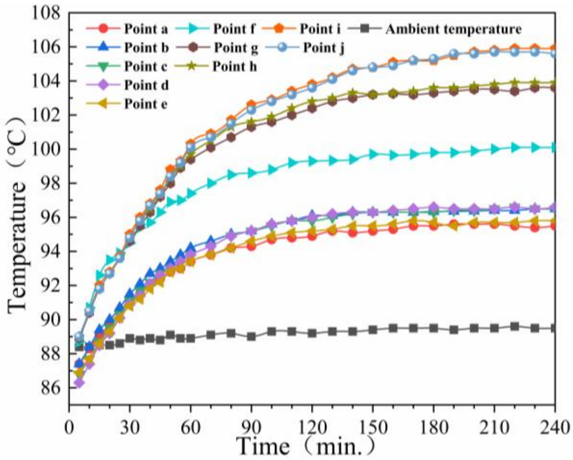

Figure 9. Temperature curves under 175A

Table 3 Comparison of experimental results and simulation results

Operating condition 1	Point 1	Point 2	Point 3	Point 4	Point 5	Point6
Average temperature (℃)	91.24	93.40	96.52	104.10	87.52	97.56
Simulated temperature(℃)	95.49	94.30	97.58	100.88	91.44	93.78
Percentage error	4.65%	0.96%	0.79%	1.10%	4.48%	3.88%

4. Analysis of the heat dissipation structure design for film capacitor

4.1 Design of the heat dissipation structure for capacitors

Inspired by the design of integration of microchannel cold plates into the film capacitor [23], an external heat dissipation structure consisting of a micro-channel liquid cold plate is proposed in this paper. Considering both space utilization and maximizing the heat dissipation area, the plate is mounted on the back of the casing. Compare to the inner cold plates design, the external design not only simplifies the assembly processes and maintenance, but also holds advantages in terms of economic feasibility and practical application. It provides a more feasible and sustainable solution to the heat dissipation challenges faced by capacitors. Through electro-thermal coupled simulation of the original capacitor, the temperature field distribution of the capacitor is obtained under ripple currents of 150 A and 175 A and an ambient temperature of 85 °C. An external heat dissipation structure with a micro-channel liquid cold plate is proposed, as shown in fig. 12. The micro-channel liquid cold plate is installed on the outer surface of the capacitor’s casing. Considering both space utilization and maximizing the heat dissipation area, the micro-channel liquid cold plate is mounted on the back of the casing. The three-dimensional model of the micro-channel liquid cold plate is illustrated in fig. 12. The dimensions of the plate are set to a length of 268 mm, width of 88 mm, and thickness of 5 mm. Inside the liquid cold plate, there is a U-shaped micro- channel with a rectangular cross-sectional area measuring 4 mm in length and 2 mm in width. Due to the fact that, in the electro-thermal coupled analysis, the highest temperature of the capacitor is near the DC terminals, the fluid inlet of the micro-channel liquid cold plate is set on the side near the DC terminals, while the other side serves as the fluid outlet.

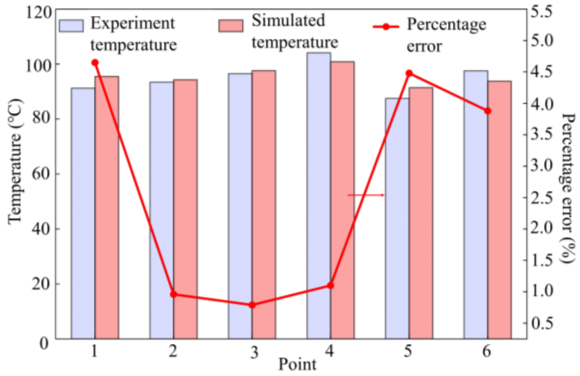

Figure10. Comparison for condition 1

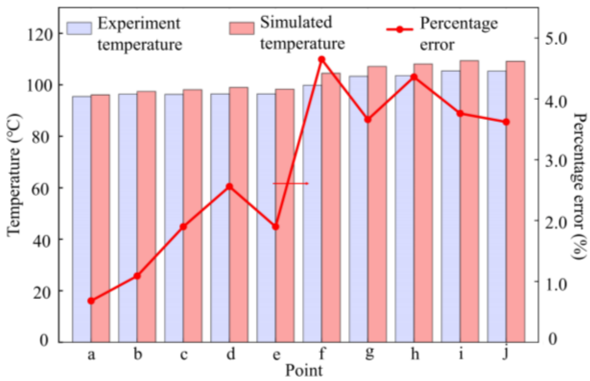

Figure11. Comparison for condition 2

4.2 Grid independence tests

The thermal performance of the capacitor with microchannel cooling plates was simulated using FLUENT. Before the FLUENT analysis, grid independence tests were conducted. The meshing method employed was polyhedral-hexahedral, and the boundary layer of the fluid domain was divided into three layers. Ensuring a model face mesh skewness of no more than 0.7 and body mesh orthogonal quality of no less than 0.2, seven groups of meshes were created, as shown in tab. 4. Fig. 13 illustrates the global temperature difference corresponding to each of the seven groups of meshes under the same operating conditions, and indicates that the grid independence curve tends to stabilize from group Ⅳ onwards. Therefore, the mesh model with serial number Ⅳ was adopted in the subsequent simulations. The final meshed model of the capacitor with cold plate under serial number Ⅳ are depicted in fig.14.

4.3 Simulation analysis of the capacitor with heat dissipation structure

Drawing on the micro-channel cooling structures of lithium batteries [24,25], it is known that the effectiveness of micro-channel cooling in lithium batteries depends on various factors. Crucial influencing factors include the cooling fluid inlet cross-sectional area, type of cooling fluid, inlet temperature of the cooling fluid, and mass flow rate of the cooling fluid. Among these factors, the first three have a more pronounced impact on temperature. This paper focuses on studying the influence of inlet mass flow on the maximum temperature of thin film capacitors without altering the heat dissipation structure. The cross-sectional area of the microchannel cooling flow path is 8 mm^2, the cooling fluid is liquid water, and the inlet temperature is 25 ℃. Ten different mass flow rates were applied to the microchannel flow path for transient simulations of the capacitor using FLUENT. The simulation parameters included 240 time steps, each with a 60-second interval, a maximum of 20 iterations, and data collection every 10 seconds. Fig. 15 illustrates the correlation between the overall highest temperature of the capacitor and the mass flow.

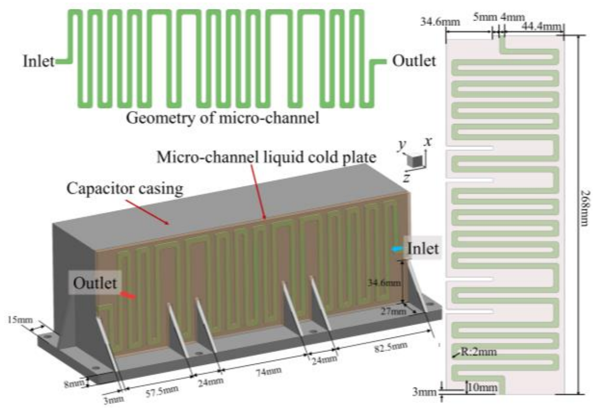

Figure 12. Modeling of heat dissipation structure

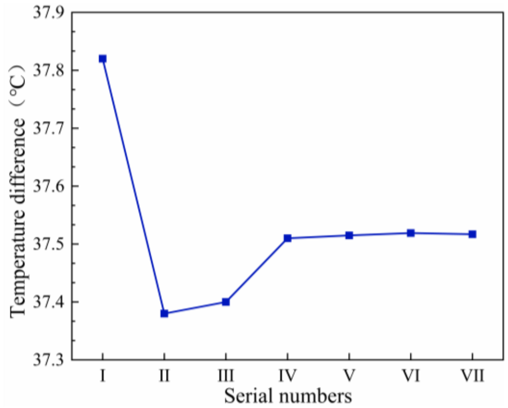

Figure 13. Tests for mesh independence

Table 4 Grid numbers in seven meshes

Serial numbers	I	II	III	IV	V	VII	VIII
Grid numbers	2359225	2869211	3447512	6579710	7124933	8650421	25779202

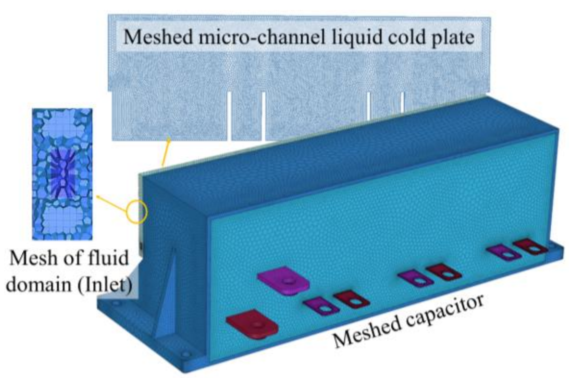

Figure 14. Meshed model of the capacitor

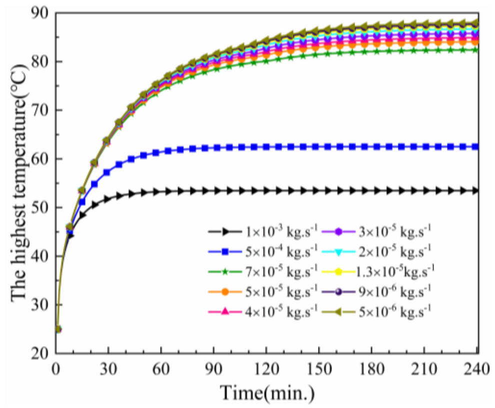

Figure 15. The overall temperature variation curve

The increase in mass flow rate can reduce the maximum temperature of the capacitor, as depicted in fig.15. In the transient simulation of 240 minutes with 10 different inlet mass flows set in this paper, when the mass flow rate is 5×10^{-6} kgs^{-1}, the capacitor's maximum temperature is 88.01 ℃. As the mass flow rate increases to 5×10^{-5} kgs^{-1}, the maximum temperature of the capacitor decreases by 3.95 ℃. With the continuous increase in the mass flow rate, the maximum temperature of the capacitor continues to decrease, but the rate of decrease gradually diminishes. When the mass flow rate increases from 5×10^{-5} kgs^{-1} to 5×10^{-4} kgs^{-1}, the maximum temperature decreases by 19.89 ℃. Increasing the mass flow rate implies consuming more energy, inevitably leading to higher operational costs. Therefore, the selected mass flow rate in the micro-channel liquid cold plate of this capacitor's heat dissipation structure is 5×10^{-4} kgs^{-1}.

At an ambient temperature of 85 °C, ripple current of 175 A, with water as the coolant and a mass flow rate into the micro-channel liquid cold plate set at 5×10^{-4} kgs^{-1} and an inlet temperature of 25 °C, the heat dissipation simulations of the two kinds of capacitors were conducted. Fig. 16 illustrates the simulation results of the heat generation in capacitor cores and the temperature distributions comparison of the capacitors with and without the external heat dissipation structure.

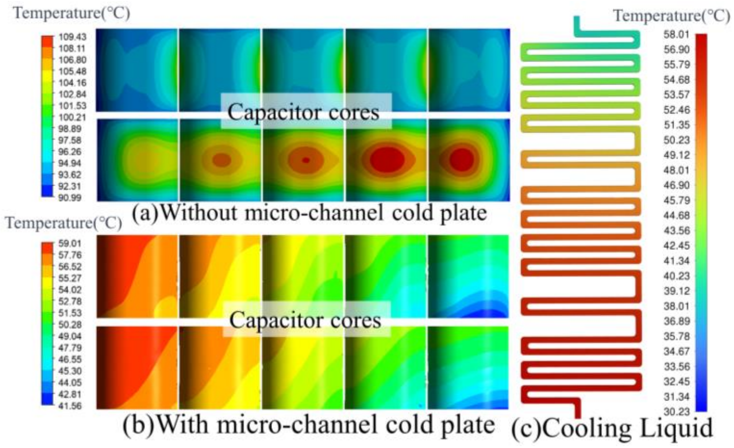

Figure16. At a ripple current of 175 A and an ambient temperature of 85 °C

It can reveal from fig. 16 that the maximum and average temperatures of the capacitor cores with the heat dissipation structure are markedly lower than those of the original capacitor cores. The maximum temperature of the cores decreases from 109.43 °C to 59.01 °C, representing a reduction of 50.42 °C or 46.08%. The heat dissipation effect is excellent compared to the original capacitor. In the capacitor without heat dissipation structure, the highest temperature region is situated on the inner walls of the two cores near the DC terminals. In contrast, the capacitor with heat dissipation structure exhibits its highest temperature on the inner walls of the cores near the cooling fluid outlet.

5. Conclusion

This paper focuses on the heat dissipation of a film capacitor in NEVs and utilizes ANSYS to establish an electric-thermal coupled simulation model for the capacitor. Additionally, a heat dissipation structure with a micro-channel liquid cold plate is designed to increase the high temperature performance of the film capacitor. Through ANSYS analysis, the temperature field distributions of the capacitor under different ripple currents were conducted. The capacitor exhibits localized high-temperature regions, with the highest temperatures concentrated at the cores near the DC terminals. Temperature rise experiments were carried out, and the results verified the ANSYS simulation. An external heat dissipation structure consisting of a micro-channel liquid cold plate is designed, and the effectiveness of the cold plate was simulated through FLUENT. The micro-channel liquid cold plate has effectively improved the heat dissipation of the capacitor. At an ambient temperature of 85°C and a ripple current of 175 A, the maximum temperature of the capacitor core is reduced by 46.08%, compared to the original capacitor. The analysis results in this study contribute to the investigation of electro-thermal coupling and temperature distribution in high-temperature film capacitors. Additionally, it provides insights for the design and optimization of the capacitor’s heat dissipation structure.

Acknowledgement

This work is sponsored by National Key R & D Program of China (No.2022YFB2502802), National Natural Science Foundation of China (No.52005318), Special Foundation for Doctoral Degree in School of Mechanical and Automotive Engineering of Shanghai University of Engineering Science, and partly sponsored by the Program for Shanghai Academic Research Leader (No.

21XD1401100) and the Project of Technical Service Platform for Noise and Vibration Evaluation and Control of New Energy Vehicles (No.18DZ2295900) at Science and Technology Commission of Shanghai Municipality, China.

Nomenclature

b_0	-The margin width of the film [m]	*Greek symbols*	
b_w	-The width of the film [m]	β	-The sheet resistance of the metal electrode layer [Ωsq^{-1}]
C	-The capacitance of the capacitor [F]	ρ	-Density of the material [kgm^{-3}]
d_m	-The thickness of the metal electrode layer [m]	*Subscripts*	
I	-Current [A]	*m*	-Metal electrode layer
i_1	-The direct current output from the battery [A]	*xm*	-The metallized film
i_2	-The current entering the inverter [A]	*Acronyms*	
i_3	-The ripple current of the capacitor [A]	AC	-Alternating Current
i_a, i_b, i_c	-Output three-phase current [A]	DC	-Direct Current
L	-Winding length [m]	ESR	-Equivalent series resistance
p	-Heating power of the metal electrode [W]	EV	-Electric vehicle
P	-Heating power of the capacitor [W]	HEV	-Hybrid electric vehicle
q_H	-The heat density of the cores [$W \cdot m^{-3}$]	IGBT	-Insulated-gate bipolar transistor
R_{xm}	-Resistance of the metallized film [Ω]	MOSFET	-Metal-oxide–semiconductor field-effect transistor
S_a,S_b, S_c	-The inverter's three-phase switching functions	NEV	-New energy vehicle
V	-The equivalent total volume of the capacitor cores [m^3]	SiC	-Silicon carbide

References

[1] Kumar A, et al., Issues, challenges and future prospects of electric vehicles: A review, International Conference on Computing, Power and Communication Technologies. IEEE, 2018, pp. 1060-1065

[2] An, Z., *et al.*, A review on lithium-ion power battery thermal management technologies and thermal safety, *Journal of Thermal Science, 26* (2017), pp. 391-412

[3] Chen, Y., *et al.*, A tutorial on high-density power module packaging, *IEEE Journal of Emerging and Selected Topics in Power Electronics, 11* (2022), pp. 2469-2486

[4] Cittanti, D., *et al.,* Analysis, design and experimental assessment of a high power density ceramic DC-link capacitor for a 800 V 550 kVA electric vehicle drive inverter, *IEEE Transactions on Industry Applications,* (2023), pp. 7078-7091

[5] Rąbkowski, Jacek, and Tadeusz Płatek., Comparison of the power losses in 1700V Si IGBT and SiC MOSFET modules including reverse conduction, 17^{th} European Conference on Power Electronics and Applications, 2015, pp. 1-10

[6] Allca-Pekarovic, A., *et al.,* Loss modeling and testing of 800 V DC bus IGBT and SiC traction inverter modules, *IEEE Transactions on Transportation Electrification,10* (2024), pp. 2923-2935

[7] Flicker, J., et al., Lifetime testing of metallized thin film capacitors for inverter applications, 39^{th} Photovoltaic Specialists Conference (PVSC), IEEE, 2013, pp. 3340-3342

[8] Wu, X., *et al.*, Advanced dielectric polymers for energy storage, *Energy Storage Materials,44* (2022), pp. 29-47

[9] Carter M A. Film capacitor for high temperature applications: U.S. Patent 6,687,115. 2004-2-3

[10] Zhou, M, *et al.*, Combining high energy efficiency and fast charge-discharge capability in novel BaTiO3-based relaxor ferroelectric ceramic for energy-storage, *Ceramics International,45*(2019), pp. 3582-3590

[11] Yang, C., et al., Fatigue- free and bending- endurable flexible Mn- doped Na0. 5Bi0. 5TiO3-BaTiO3- BiFeO3 film capacitor with an ultrahigh energy storage performance, *Advanced Energy Materials,9* (2019), pp. 1803949

[12] Cui, Y, et al., Research on the influence of safety film on the thermal field distribution of metallized film capacitors, International Symposium on Insulation and Discharge Computation for Power Equipment, Singapore: Springer Nature Singapore, 2023, pp. 447-455

[13] Xu, S, *et al.*, Strain engineering of energy storage performance in relaxor ferroelectric thin film capacitors, *Advanced Theory and Simulations, 5* (2022), pp. 2100324

[14] Li, J, *et al.*, Biaxially oriented films of grafted-polypropylene with giant energy density and high efficiency at 125° C, *Journal of Materials Chemistry A,11* (2023), pp. 10659-10668

[15] Wu, C, *et al.*, Flexible temperature- invariant polymer dielectrics with large bandgap, *Advanced Materials,32* (2020), pp.2000499

[16] MacDonald JR, et al., High energy density capacitors, IEEE Electrical Insulation Conference. IEEE, 2009, pp.306-309

[17] Zhang C, *et al.*, Evolution characteristics of DC breakdown for biaxially oriented polypropylene films, *IEEE Transactions on Dielectrics and Electrical Insulation,30* (2023), pp. 1188-1196

[18] Yao, R, et al., Lifetime analysis of metallized polypropylene capacitors in modular multilevel converter based on finite element method, *IEEE Journal of Emerging and Selected Topics in Power Electronics, 9*(2020), pp. 4248-4259

[19] Kong, Michael G., and Yuen-Pen Lee., Electrically induced heat dissipation in metallized film capacitors, *IEEE transactions on dielectrics and electrical insulation, 11* (2004), pp. 1007-1013

[20] Reimers, J, *et al.*, Automotive traction inverters: Current status and future trends, *IEEE Transactions on Vehicular Technology, 68* (2019), pp.3337-3350

[21] Topolewski JN, *et al.*, Cold plate with integrated DC link capacitor for cooling thereof: U.S. Patent 9,615,490. 2017-4-4

[22] Tai, Y, *et al.*, Failure mechanism and life estimate of metallized film capacitor under high temperature and humidity, *Microelectronics Reliability, 137* (2022), pp. 114755

[23] Huang, L, *et al.*, Numerical investigation and optimization on thermal management of a DC-bus film capacitor in electric vehicle using microchannel cooling plates, *Applied Thermal Engineering, 244*(2024), pp. 122695

[24] Zhen GONGa., *et al.*, A study of the effects of the micro-channel cold plate on the cooling performance of battery thermal management systems, *Thermal Science,26*(2022) , pp.1503-1517

[25] Liu, WZ., *et al.*, Microchannel topology optimization based on enhanced heat transfer mechanism, *Thermal Science*, *28*(2024), pp.611-626

Submitted: 27.6.2024
Revised: 18.9.2024.
Accepted: 22.9.2024.